G-DIF: A geospatial data integration framework to rapidly estimate post-earthquake damage

Sabine Loos[a], M.EERI, **David Lallemant**[b], M.EERI, **Jack Baker**[a], M.EERI, **Jamie McCaughey**[e], **Sang-Ho Yun**[c], **Nama Budhathoki**[d], **Feroz Khan**[b], **Ritika Singh**[d]

While unprecedented amounts of building damage data are now produced after earthquakes, stakeholders do not have a systematic method to synthesize and evaluate damage information, thus leaving many datasets unused. We propose a Geospatial Data Integration Framework (G-DIF) that employs regression kriging to combine a sparse sample of accurate field surveys with spatially exhaustive, though uncertain, damage data from forecasts or remote sensing. The framework can be implemented after an earthquake to produce a spatially-distributed estimate of damage and, importantly, its uncertainty. An example application with real data collected after the 2015 Nepal earthquake illustrates how regression kriging can combine a diversity of datasets–and downweight uninformative sources–reflecting its ability to accommodate context-specific variations in data type and quality. Through a sensitivity analysis on the number of field surveys, we demonstrate that with only a few surveys, this method can provide more accurate results than a standard engineering forecast.

INTRODUCTION

From rapid engineering forecasts to crowdsourced maps, unprecedented amounts of building damage data are now being produced after earthquakes. The 2010 Haiti earthquake was the first time that response and recovery stakeholders had access to this amount of damage data, due to both technological advancements in remote sensing data acquisition and mandates to make that data openly available after major disasters (Corbane et al., 2011; Kerle and Hoffman, 2013). In fact, after 2010 there was a spike in the number of damage-related maps posted on ReliefWeb—a global information sharing site devoted to humanitarian disasters—in response to

[a] Stanford University, Stanford, CA 94305
[b] Earth Observatory of Singapore, Nanyang Technological University, Singapore
[c] Jet Propulsion Laboratory, California Institute of Technology, 4800 Oak Grove Drive, Pasadena, CA 91109
[d] Kathmandu Living Labs, Kathmandu, Nepal
[e] Institute for Environmental Decisions, Dept. Environmental Systems Science, ETH Zürich, Zürich, Switzerland

1

major earthquakes despite having similar estimated economic damages as earlier events (Figure 1).
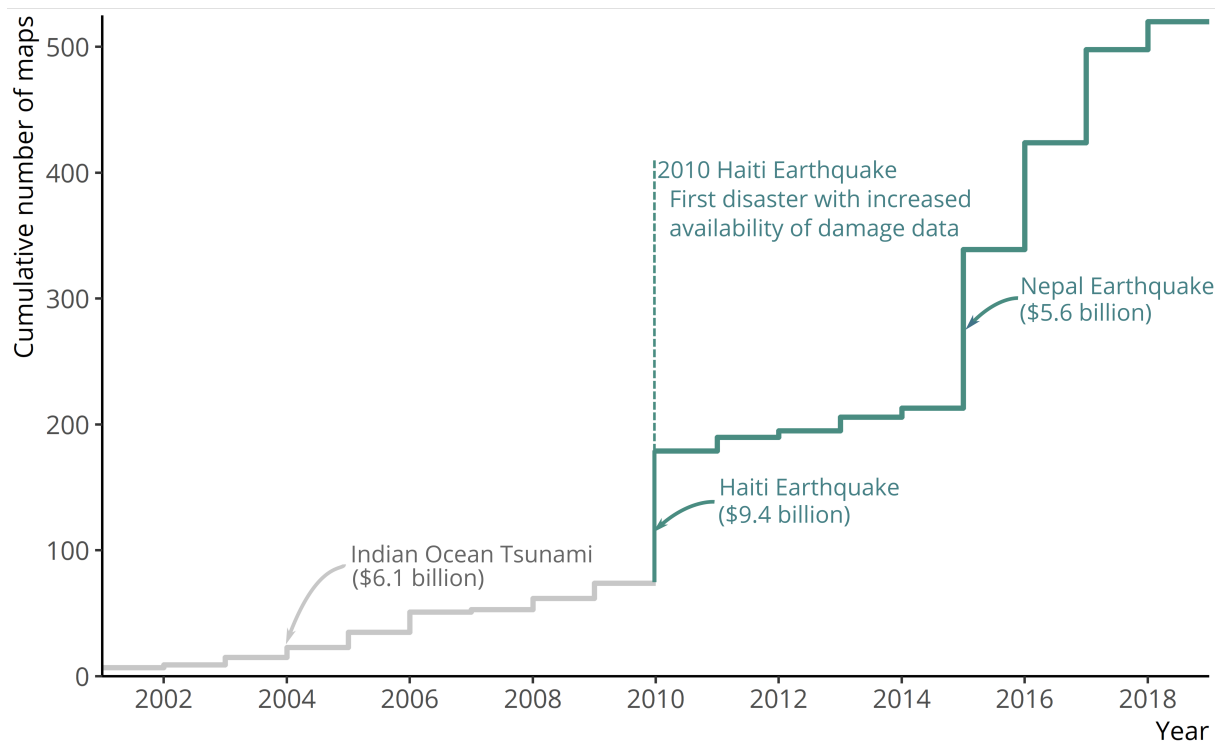
Figure 1. The number of damage-related maps posted on ReliefWeb, a disaster information sharing site, has increased since the 2010 Haiti earthquake. We would expect a similar number of maps for major events with similar estimated economic damages (shown in 2019 USD). The number of maps were scraped from ReliefWeb and economic damages were retrieved from EM-DAT (United Nations Office for the Coordination of Humanitarian Affairs, 2019; Université catholique de Louvain (UCL) - CRED and Guha-Sapir)

Counterintuitively, the increase in data is problematic since stakeholders–such as affected governments, multilateral donor organizations, and humanitarian organizations–receive a barrage of information and maps with unverified competing damage estimates (Kerle, 2013). Often, data from new and untested methods are left unused when decisions need to be made quickly (Hunt and Specht, 2019). Stakeholders do not have a systematic method to quickly assess the accuracy or synthesize these data sources. Furthermore, it is common for damage to be quantified using metrics that are not usable for stakeholders to make crucial decisions within weeks of an earthquake (Bhattacharjee et al., 2018). For example, in as little as two weeks, the affected government uses damage data to estimate total losses for the Post Disaster Needs Assessments (PDNA) to request recovery aid. It is unclear how to 1) translate multiple remotely-sensed damage maps that show damage intensity per pixel, like the maps shown in Kerle and Hoffman (2013), to usable metrics to estimate loss and 2) know which map is most accurate. If damage

estimates are inaccurate in the PDNA, the affected government could under or overestimate the amount of aid requested—and subsequently distributed—for recovery. Because of these issues, many damage data are left unused. This paper outlines a Geospatial Data Integration Framework (G-DIF) to systematically integrate multiple sources of damage data into a single spatially distributed estimate of damage with quantified uncertainty to ease decision-making and improve the accuracy of post-earthquake damage estimates.

Integrating post-earthquake damage data is challenging since they are produced at different times with varying geospatial coverages, formats, and levels of uncertainty. While a few research studies have attempted to improve the accuracy of remote sensing and crowdsourced damage data, none have developed generalized methods to combine multiple data sources into a single, high-resolution, and spatially distributed estimate of building damage. For example, Booth et al. (2011) used Bayesian analysis to update the ratio of collapsed buildings in an affected area from manual assessments of satellite imagery with additional satellite assessments and field surveys after the 2010 Haiti earthquake but produced collapse probability distributions for four low-resolution land-use classes rather than high-resolution spatial estimates. Alternatively, some studies treat post-earthquake damage data as inputs and validation for vulnerability curves within an engineering forecast (e.g. Gunasekera et al., 2018; Huyck, 2015), but do not update the final damage estimate itself. Rather than estimating damage, some studies have used multiple damage data to develop maps of shaking intensity (e.g. Monfort et al., 2019). Finally, Lallemant and Kiremidjian (2013) applied cokriging to integrate a crowdsourced assessment with a set of field surveys, but this method was not generalized to incorporate multiple damage data sources.

As opposed to existing methods, which rely on only one to two damage datasets, we propose a framework that is able to integrate multiple heterogeneous data sources to produce a single spatial damage prediction in the weeks after an earthquake. Specifically, the geostatistical model, regression kriging, implemented in G-DIF requires a limited sample of primary damage data from field surveys, which are accurate but have low spatial coverage, to predict damage using secondary damage data, which have lower accuracy but higher spatial coverage. Within this framework, we employ a geostatistical integration method, since damage between nearby buildings are likely correlated within the range of spatial correlation of ground motion because of similarities in construction age and material, local soil conditions, and multiple other factors (Shome et al., 2012). By modeling this spatial correlation parametrically, G-DIF does not rely on large field survey samples as training data, unlike most machine learning models.

Therefore, instead of relying on a model that is built with training data from one location and may not transfer well between different built environments and different data sources, G-DIF can be be developed after an event using its specific data, leading to locally calibrated damage estimates. Because of these features, similar geostatistical techniques have been previously applied to integrate data in other fields such as for mapping atmospheric optical thickness (e.g. Chatterjee et al., 2010) and soil properties (e.g. Hengl et al., 2004; Thompson et al., 2010).

In this paper, we illustrate the implementation of the framework with an example application using real damage data collected after the 2015 Nepal Earthquake. In this example, we show how G-DIF produces a single map of damage and a map of the estimation uncertainty, which can be used to model economic losses and guide further field surveying, respectively. Compared to traditional methods of rapidly estimating post-earthquake damage, G-DIF results in a damage estimate with lower overall error, higher resolution, and is specific to each context.

POST-EARTHQUAKE DAMAGE DATA SUITED FOR G-DIF

G-DIF makes use of two types of damage information: primary measurement data with high accuracy and sparse spatial coverage, plus secondary proxy data with low accuracy and dense spatial coverage. Examples of primary data include field surveys of damage and secondary data includes engineering forecasts, remotely-sensed proxies, or relevant geospatial covariates from before or after the event (e.g. intensity or elevation). All information is assumed to be numerical (e.g. collapse rate) rather than descriptive (e.g. social media posts). In this section, we outline the time of availability and format of the damage data suited for G-DIF, as shown in Figure 2.

FIELD SURVEYS

Field surveys of damaged buildings are often conducted following earthquakes. These include surveys conducted by reconnaissance teams to understand the scale and type of building damage, rapid engineering safety evaluations to inform people of the safety of reoccupying buildings, and detailed, recovery-oriented surveys as time progresses (Earthquake Engineering Research Institute, 2015; Lallemant et al., 2017). These field surveys include an evaluation of the level of damage for each inspected building. The two most prevalent methods to assign damage levels are the ATC-20 methodology and the EMS-98 grading system, where engineers classify building damage in damage states or grades, respectively, based on descriptive damage conditions (Applied Technology Council, 1989; Grünthal, 1998). Since engineers inspect
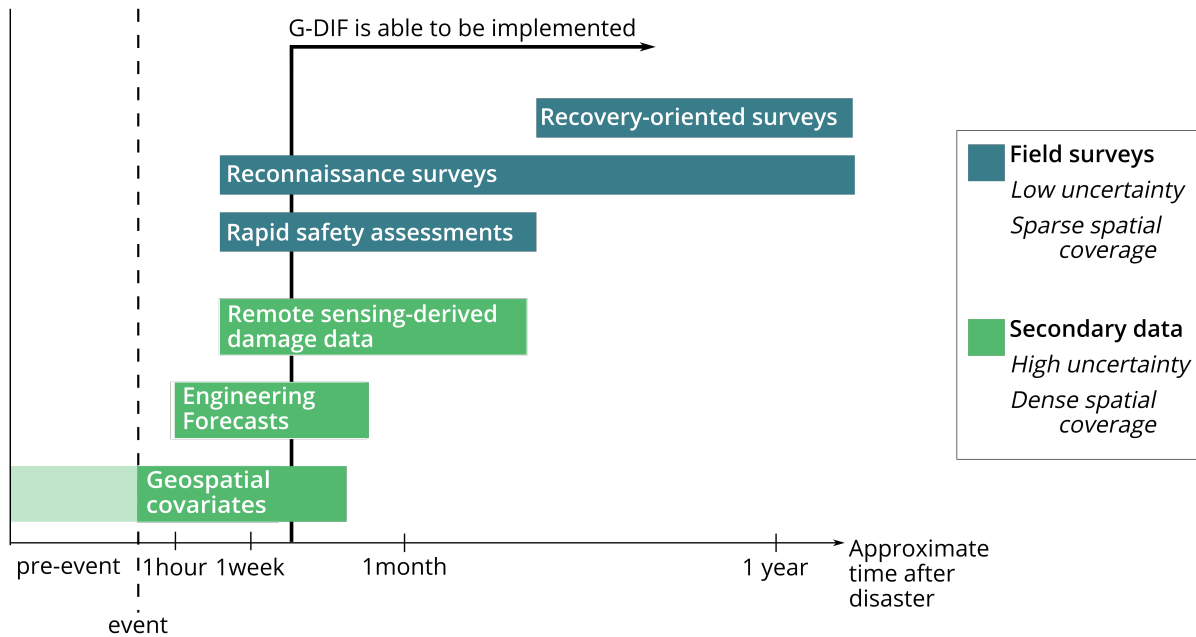
Figure 2. Timeline of availability of post-earthquake damage data suited for G-DIF based on Lallemant et al. (2017)'s review of damage assessments. Data sources with lower accuracy but dense spatial coverage are available soonest after an earthquake. Once a limited sample of field surveys are collected, enough data is available for G-DIF. The time to collect a sufficient amount of field surveys can vary by region (in Nepal, it could feasibly be done in a couple of weeks), however, a couple of weeks is sufficient for early recovery decisions.

each building from the ground, field survey assessments are the most accurate measurement of damage relative to other damage data. The timing of early field surveys varies between disasters—past examples from the REACH survey, the government, and reconnaissance teams have shown organized surveys to be conducted in the first 6 weeks (Shelter Cluster Nepal, 2015; Lallemant et al., 2017; Earthquake Engineering Research Institute, 2015). While full coverage of on-the-ground surveys takes months to even years after a major event, G-DIF leverages these early surveys to provide calibration of predictions and constraints at the survey locations.

ENGINEERING FORECASTS

Engineering forecasts are near-real-time predictions of regional impact available within hours, as soon as a map of shaking intensity can be derived from the magnitude and location of the earthquake source (Jaiswal et al., 2009). Multiple global systems exist, the most widely used being the Prompt Assessment of Global Earthquakes for Response (PAGER) system (Jaiswal and Wald, 2011). These systems typically use an analytical or empirical model that relates shaking intensity to impact measures such as building damage, casualties, or economic loss. These

5

models usually rely on information on the earthquake shaking in terms of peak ground motion or intensity, building and population exposure, and fragility functions (Erdik et al., 2014). While systems like PAGER aggregate their models to country-level impact estimates, alternative systems, such as the Quake Loss Assessment for Response and Mitigation (QLARM), provide spatially distributed model predictions (Trendafiloski et al., 2009). Since engineering forecasts are model-based, rather than observation-based, these predictions are inherently uncertain, especially in regions with limited seismic stations and building inventory data (Wald et al., 2012; Erdik et al., 2014).

REMOTE SENSING-DERIVED DAMAGE DATA

Remote sensing-derived damage data are observations related to damage, retrieved from earth observation technologies such as sensors mounted on satellites, aircraft, or unmanned aerial vehicles. These signals can be interpreted automatically through computer algorithms or manually by humans, each with a range of formats (Dong and Shan, 2013; Kerle, 2013). Depending on the interpretation method, the data are either damage proxies, which provide an idea of damage intensity, or assessments, which provide direct measurements of damage. For example, the Advanced Rapid Imaging and Analysis project at NASA's Jet Propulsion Laboratory and California Institute of Technology produce damage proxy maps (DPM) for major disasters based on an automatic change detection between two pairs of images from Interferometric synthetic-aperture radar (InSAR) data, thus providing a measure of intensity (Yun et al., 2015). Alternatively, digital humanitarian groups, such as Humanitarian OpenStreetMap Team (HOT) or the Global Earth Observation-Catastrophe Assessment Network (GEO-CAN), have manually identified damaged and collapsed buildings in optical satellite and aerial imagery, respectively (Westrope et al., 2014; Loos et al., 2018; Ghosh et al., 2011). The availability of remote sensing-derived damage data depends on the retrieval of the underlying remote sensing data—typically within a few days to a couple of weeks (Dong and Shan, 2013; Lallemant et al., 2017). While remotely sensing damage data have denser spatial coverage than field surveys, these estimates have varying accuracy depending on the type of imagery or interpretation used (Loos et al., 2018; Dong and Shan, 2013; Monfort et al., 2019).

GEOSPATIAL DATA INTEGRATION FRAMEWORK

Our goal is to estimate the true building damage, Z, which is the assigned damage grade for a building *from a field survey*. We formulate the true damage as a function of location, s, so $Z(s)$ is a continuous variable. The region is discretized into a grid, so that $Z(s)$ is defined at a countable number of locations. When the grid dimension encompasses multiple buildings, Z can be defined as the average damage grade (hereon referred to as mean damage) of the buildings or the fraction of buildings that fall within a given grade.

We consider the true damage as a random spatial process composed of two parts: 1) the mean surface, which is the average damage throughout space and 2) small-scale fluctuations around the mean surface. In the case of earthquake-induced building damage, the mean surface will exhibit a general trend in space, because of characteristics such as shaking intensity that have large-scale spatial variation. We model this trend parametrically. We expect the small-scale fluctuations (hereon the residuals) to exist, resulting from smaller scale similarities in characteristics such as construction characteristics and local soil conditions. Because of the small-scale similarities, we model the residuals as stochastic and spatially auto-correlated, or correlated with itself between two locations.

The true building damage Z at a single location s, can therefore be represented as the sum of the trend, $m(s)$, and stochastic residual, $\varepsilon(s)$,

$$Z(s) = m(s) + \varepsilon(s). \tag{1}$$

To illustrate, consider two communities A and B—community A is closer to the earthquake source and experienced greater shaking, and therefore damage, than the more distant community B. The average difference in damage between A and B is represented by the trend, $m(s)$. Beyond that, the buildings in the grids in and around A are constructed similarly—built with the same material in the same year—causing similar damage. The local similarities in damage surrounding a grid is represented by the spatially correlated residual $\varepsilon(s)$.

Note that $Z(s)$ is defined as the true damage, since a field surveyed assessment is relatively the most accurate measurement of damage available after an earthquake. Uncertainty in a field survey still exists due to the subjectivity of the surveyor, and the additional uncertainty introduced from aggregating the surveys to a grid. Here, however, we consider $Z(s)$ to be exact and only account for the uncertainty in the estimation of the trend and the spatially-correlated residuals.

G-DIF capitalizes on 1) the correlation between the sparse field surveys and secondary damage data to estimate the trend and 2) the auto-correlation between the field surveys to estimate the residuals. The geostatistical data integration model implemented in G-DIF is regression kriging (also known as residual kriging), a multivariate geostatistical regression technique, which consists of two separate models for the trend and the residuals (Odeh et al., 1994). Separate modeling of the trend and residuals allows for alternative regressions that consider nonlinear relationships between primary and secondary data and separate interpretation of each model's results. The main steps of the framework are in Figure 3.
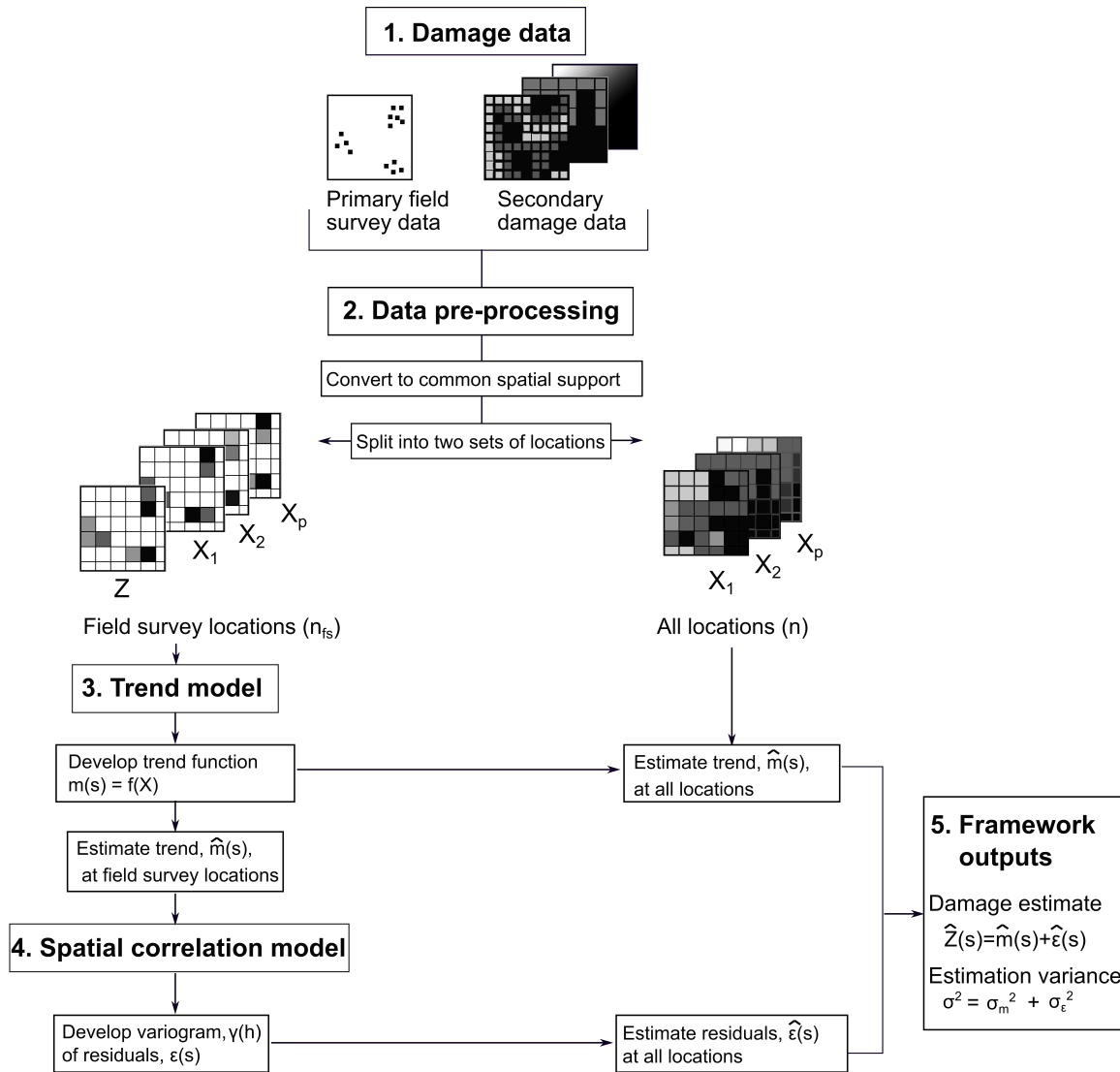
Figure 3. G-DIF steps to produce spatial estimates of regional damage.

DATA PRE-PROCESSING

We separate the input data for G-DIF into two sets of locations. There are p secondary datasets, $X_1 \ldots X_p$, that are spatially exhaustive and available at all n locations with an additional set of primary field survey data at a subset of n_{fs} locations. The collocated primary and secondary data at the n_{fs} field survey locations are used for developing a regression function, which is then used to estimate the trend at all n locations. Similarly, the spatial correlation model is developed using the n_{fs} field locations. Generally, the set of field surveys should be large enough to build a regression model for the trend ($n_{fs} >> p$) and have samples at each damage level and varying distances from each other. In this paper, we assume that the set of field surveys include observations of the full range of damage levels and are carried out at random grids distributed throughout the spatial domain in order to produce unbiased estimates of the trend and variogram (this assumption has important implications for survey sampling, which we revisit in the sensitivity analysis and conclusion sections). The vector of field surveys ($\mathbf{Z}$) and matrix of secondary datasets ($\mathbf{X}$) for model development are

$$
\mathbf{Z} = \begin{bmatrix} Z(s_1) \\ \vdots \\ Z(s_{n_{fs}}) \end{bmatrix} \quad \mathbf{X} = \begin{bmatrix} X_1(s_1) & \ldots & X_p(s_1) \\ \vdots & \ldots & \vdots \\ X_1(s_{n_{fs}}) & \ldots & X_p(s_{n_{fs}}) \end{bmatrix}.
$$

To model the trend, we develop a regression function, f, which predicts the true damage at the field survey locations, $\mathbf{Z}$, as a function of the damage from the secondary data, $\mathbf{X}$. We use the developed regression function to estimate the trend at a single, unknown location, s_0:

$$
\hat{m}(s_0) = f(\mathbf{X}(s_0)). \tag{2}
$$

TREND MODEL

The function f is the modeler's choice and will generally be earthquake-specific. Because the choice of trend model is likely to be dependent on the data available, it is important to develop this function manually to obtain accurate estimates of the final damage. It is common to apply ordinary least squares (OLS) for trend estimation. Alternatively, generalized least squares (GLS), which weights observations by their spatial covariance, accounts for spatial correlation in the residuals and leads to an unbiased estimate of the coefficient. The use of GLS leads to results most similar to estimating the trend and residual simultaneously, as with universal kriging (Hengl et al., 2003; Chiles and Delfiner, 2012). In either formulation, both linear and nonlinear

9

least-squares regression functions can be applied. Other functions such as general additive models, regression trees, and artificial neural networks have also been explored within this general approach (McBratney et al., 2000; Grujic, 2017; Motaghian and Mohammadi, 2011). In addition, separate trend models can be developed for different regions that have varying coverage of secondary data. This could be the case for imagery-based damage data that can be limited in geographical extent, which we demonstrate in our application to Nepal.

SPATIAL CORRELATION MODEL

With the developed trend function we estimate the trend at all n locations and calculate the residuals at each of the n_{fs} field surveyed locations:

$$\varepsilon(s_\alpha) = Z(s_\alpha) - \hat{m}(s_\alpha), \qquad \text{for } \alpha = 1...n_{fs}. \tag{3}$$

Using the calculated residuals, we perform ordinary kriging to estimate the residuals at the unknown locations using a spatial correlation model. The estimated residual at a single, unknown location is the weighted sum of the known residuals from the field surveyed locations

$$\hat{\varepsilon}(s_0) = \sum_{\alpha=1}^{n_{fs}} \lambda_\alpha(s) \cdot \varepsilon(s_\alpha) \tag{4}$$

where λ_α are the kriging weights.

We solve for the kriging weights, $\boldsymbol{\lambda} = \lambda_\alpha \ldots \lambda_{n_{fs}}$, by minimizing the estimation variance at the surveyed locations and placing a constraint on the sum of the weights to equal one to satisfy the unbiasedness conditions assumed with ordinary kriging (Chiles and Delfiner, 2012).

$$\min_{\lambda_1,...,\lambda_{n_{fs}}} \text{var}(\hat{\varepsilon}(s_\alpha) - \varepsilon(s_\alpha)) + 2\nu(\sum_{\alpha=1}^{n_{fs}} \lambda_\alpha - 1). \tag{5}$$

We obtain the $\boldsymbol{\lambda}$ that minimizes Equation 5 by introducing a Lagrange multiplier ν and setting the function's partial derivatives with respect to $\boldsymbol{\lambda}$ and ν equal to zero. This results in the following ordinary kriging system of $n_{fs} + 1$ equations with $n_{fs} + 1$ unknowns ($\boldsymbol{\lambda}$ and ν):

$$\begin{bmatrix} \underset{n_{fs} \times n_{fs}}{\mathbf{C}} & \underset{n_{fs} \times 1}{\mathbf{1}} \\ \underset{1 \times n_{fs}}{\mathbf{1}^\top} & 0 \end{bmatrix} \begin{bmatrix} \underset{n_{fs} \times 1}{\boldsymbol{\lambda}} \\ \nu \end{bmatrix} = \begin{bmatrix} \underset{n_{fs} \times 1}{\mathbf{C}_0} \\ 1 \end{bmatrix}, \tag{6}$$

where $\mathbf{C}$ is the auto-covariance matrix between the known residuals and $\mathbf{C}_0$ is the covariance between the new estimation location and all field survey locations. Here, we assume second-order stationarity of the residuals, meaning the autocovariance is the same for any two points

10

based on their separation distance, h, and irrespective of their location. The auto-covariance $\mathbf{C}$ is derived from a variogram, a concept similar to the correlation models used for ground-motion intensities (Boore et al., 2003; Goda and Hong, 2008; Jayaram and Baker, 2009). The variogram is a theoretical parametric model of spatial correlation that relates the separation distance h between field surveyed locations and the dissimilarity of their residuals. Dissimilarity in the variogram is quantified using half the variance, or the empirical semivariance

$$\gamma(h) = \frac{1}{2}\text{var}\big[\varepsilon(s) - \varepsilon(s + h)\big] = \frac{1}{2}\mathbb{E}\big[\{\varepsilon(s) - \varepsilon(s + h)\}^2\big] \tag{7}$$

where h is the euclidean distance. A theoretical variogram is then fit through all (γ, h) pairs. Selection of an appropriate theoretical variogram should again be based on the lowest error from cross-validation (Oliver and Webster, 2014).

DAMAGE AND UNCERTAINTY ESTIMATE

The final damage estimate at a single location is obtained by adding together the estimated trend and residuals from Equations 2 and 4, respectively, as shown in Equation 1

$$\hat{Z}(s_0) = f(\mathbf{X}(s_0)) + \sum_{\alpha=1}^{n_{fs}} \lambda_\alpha(s) \cdot \varepsilon(s_\alpha). \tag{8}$$

Once we develop the final damage estimate for all locations, $\hat{Z}$, it can be used to estimate further decision variables (i.e. the spatial distribution of economic losses).

In addition, this method provides the variance of the damage estimate, $\hat{\sigma}^2(s_0)$, which is the sum of the individual variances from estimating the trend, $\hat{\sigma}_m^2(s_0)$, and kriging the residuals, $\hat{\sigma}_\varepsilon^2(s_0)$.

$$\hat{\sigma}^2(s_0) = \hat{\sigma}_m^2(s_0) + \hat{\sigma}_\varepsilon^2(s_0). \tag{9}$$

The estimation variance can be used to propagate uncertainty in further loss estimates or to guide where to carry out additional field surveys.

APPLICATION TO THE 2015 NEPAL EARTHQUAKE

In this section, we demonstrate the applicability of G-DIF by using real data produced after the 2015 $\text{M}_\text{w}7.8$ Nepal earthquake to estimate damage over the 11 heavily affected and mostly rural districts outside of Kathmandu Valley. We assume this model would have been applied approximately two to four weeks following an earthquake (i.e., the vertical line in Figure 2)

when enough field surveys are available to implement G-DIF. For this example, we use field surveys at 100 random locations plus representative data sources for each type of secondary damage data. We present this case study in order of the flowchart of Figure 3.

1. DAMAGE DATA

The measurement unit and spatial support of each input data used in this case study are listed in Table 1.

Table 1. Data from the 2015 Nepal earthquake used in the application of G-DIF

Damage data category	Dataset used in case study	Measurement Unit	Spatial Support
Field surveys	EMS-98 field surveys (Z)	Damage grade	Building-level
Engineering forecast	Self-developed (X_1)	Mean damage ratio	1km grid
Remote sensing proxy	InSAR-based damage proxy map (X_2)	Damage proxy map value	30m grid
Relevant geospatial covariates	ShakeMap (X_3)	Modified Mercalli Intensity	1.75km grid
	Digital Elevation Model (X_4)	Elevation (m)	90m grid

The damage survey data for this case study come from the Earthquake Housing Damage and Characteristics Survey commissioned by the Government of Nepal and completed by July 2016 (http://eq2015.npc.gov.np/#/). The purpose of that survey was to identify rural households that would be eligible beneficiaries for the Earthquake Housing Reconstruction Program and was therefore carried out in the 11 rural most-affected districts, not including the three districts in Kathmandu Valley (Nepal Earthquake Housing Reconstruction Multi-Donor Trust Fund, 2016). In this survey, trained engineers used the EMS-98 damage grading system to classify a census of 751,799 buildings in these districts into a damage grade from 1 (negligible to slight damage) to 5 (collapse). While this exhaustive survey was completed a year after the earthquake, we consider only a random sample of 100 locations in order to replicate what would be available rapidly after an event.

We developed an engineering forecast dataset with similar methods and quality to engineering forecasts available after earthquakes in countries with limited building inventory data. We use fragility curves from Nepal's National Society of Earthquake Technology to relate the peak ground acceleration from the latest ShakeMap to damage ratios for masonry (mud and cement mortared), reinforced concrete, and wood structures (JICA, 2002; Worden et al., 2018). The exposure is defined using population estimates from the LandScan 2011 High Resolution Global Population Dataset and ratios of each construction type available at the district-level in Nepal's 2011 census (Bright et al., 2012). Given the estimated number of buildings, the estimated distribution of each construction type, and the fragility curve for each construction type, we compute

12

the mean damage ratio per grid.

For the remote sensing proxy, we use NASA's damage proxy map (DPM) (Yun et al., 2015). NASA has consistently produced a DPM after major disasters since the February 2011 M6.3 Christchurch earthquake, making it a relevant remote sensing proxy to include in this study. The DPM algorithm takes the difference between two InSAR coherence (or similarity) maps: one from before the earthquake and one spanning the earthquake. The DPM value in each pixel (which ranges -1 to 1) represents anomalous change due to the earthquake, as opposed to background changes (noise) that existed in the pre-earthquake pair coherence.

We also consider two geospatial covariates that are available after earthquakes and relate to the trend in damage: the Modified Mercalli Intensity from the ShakeMap (Worden and Wald, 2016), and a Digital Elevation Model (DEM) derived from the Shuttle Radar Topography Mission (Jarvis et al., 2008; Farr et al., 2007). While elevation may not directly cause earthquake damage, it could serve as a proxy for other factors such construction quality in remote areas or landslide occurrence. The use of elevation data for the application of G-DIF in Nepal demonstrates how the trend model down-weights secondary datasets that are poor proxies for damage, as shown in the modeling results for the trend (Section 4.3).

2. DATA PRE-PROCESSING AND EXPLORATION

We discretize each dataset to a common grid of $0.0028° \times 0.0028°(\sim 290\text{m} \times 290\text{m})$, resulting in a study area with 80,200 grid points. We use this resolution to remove any personal identifiable information, ensuring that more than one building is within each grid. The 11 considered districts are mostly rural, so there are nine buildings per grid on average (though 0.25% have 100 or more buildings).

The true damage from the field surveys, Z, is the mean damage grade of all buildings within each grid. Out of 80,200 grids that contain buildings, we randomly selected 100 grids (containing 1056 buildings) as the set of locations that engineers could survey in the field. From here on, we refer to the subset of grids as the field surveyed locations.

Exploratory analysis shows a positive relationship between the true damage and the secondary damage data as exhibited in the moving average curves in the left column of the matrix in Figure 4. Specifically, the engineering forecast, shaking intensity, and elevation are linearly related to the true damage, while the DPM shows a slightly nonlinear relationship. The form of these discovered relationships should be considered when deciding on which trend model to

13
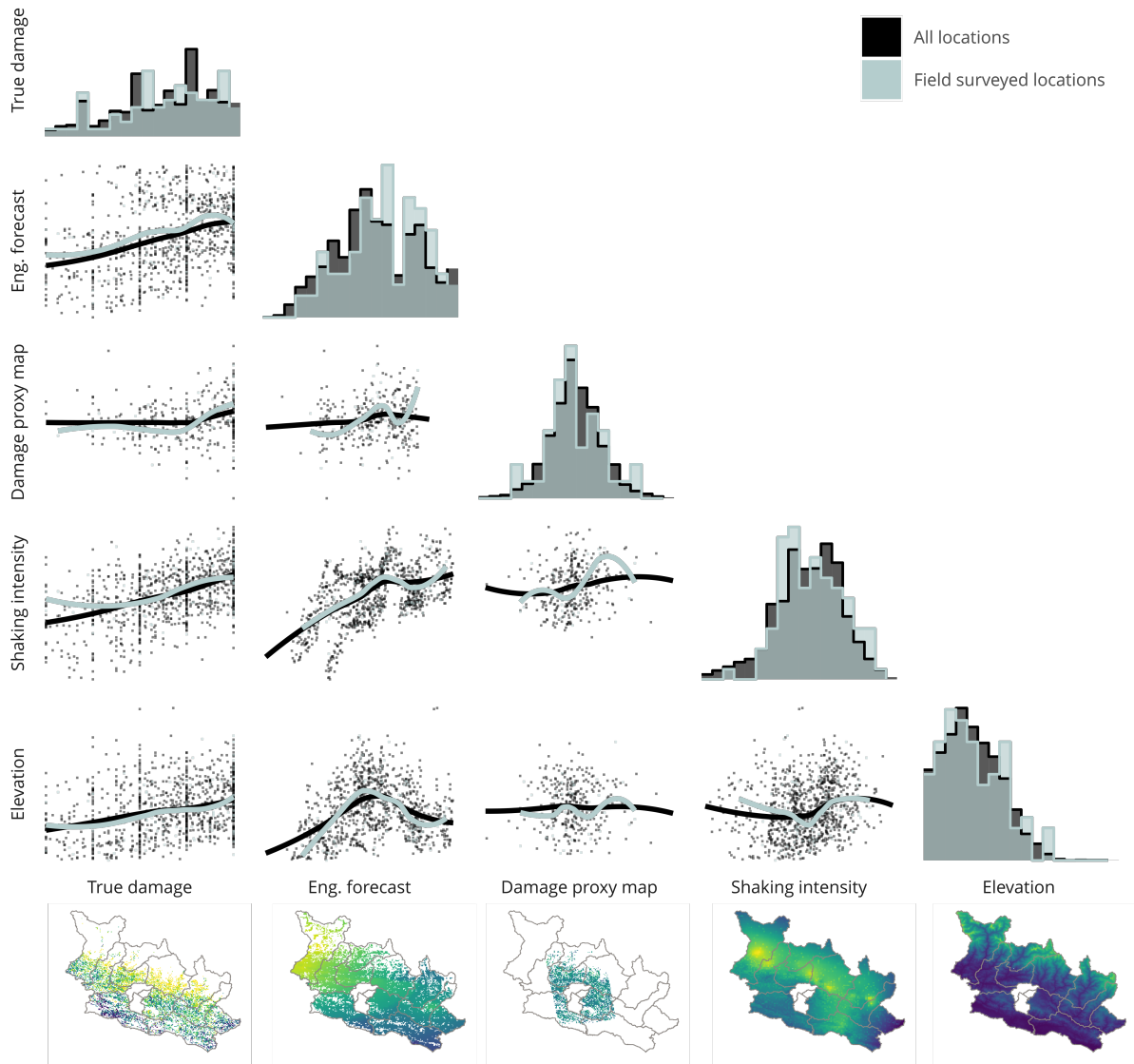
Figure 4. Summary of true damage from primary field survey and secondary damage data at all locations ($n = 80{,}200$) and the subset of field surveyed locations ($n_p = 100$). The diagonal shows histograms of each dataset, the scatter plots show relationships between datasets (including a moving average estimate), and the bottom row maps the spatial patterns of each data set (with warm colors indicating larger values). The left column of scatter plots highlights relationships between primary and secondary data.

use.

3. TREND MODEL

Based on our observations of linearity between variables, we used a linear least squares regression as the functional relationship between the true damage and each secondary damage data

$$\hat{m}(s_0) = \sum_{k=0}^{p} \hat{\beta}_k \cdot X_k(s_0) \tag{10}$$

where X_0 is a vector of ones to estimate the intercept. We estimate the coefficient for each secondary damage data, $\hat{\beta}_k$, through either ordinary least squares (OLS) regression or generalized least squares (GLS) regression. We select the regression function that results in the least root mean squared error, which is OLS regression in this example. We also build two trend models for areas with and without DPM values, since the DPM covers about 40% of the considered region (more details are in the Appendix). We compute the variance inflation factor (VIF) for each secondary data variable to assess whether multicollinearity exists (James et al., 2013), but find that the VIF's for each variable are below two–a low value that indicates multicollinearity is not a problem with these data.

Building a trend model with the data at the field surveyed locations has two advantages. First, the function in Equation 10 translates the numerous secondary damage data with differing units of measurement (e.g., shaking amplitude, elevation, an arbitrary numerical scale for DPM) into a collective unit, the mean damage grade, that has value for regional loss estimates and other decision-making.

The second advantage of the trend model is that the modeler does not need to subjectively weight the importance of each secondary damage data, instead allowing the data to determine the importance of each dataset through the model coefficients. By examining each $\hat{\beta}_k$ and its standard error, we observe which secondary dataset provides additional value in modeling the trend. For example, in Figure 5a, we see the digital elevation model (DEM) has close to a zero coefficient in the estimated trend, signifying the DEM has little additional effect on the trend estimate when we account for the other secondary damage data. These coefficients are comparable since we normalize all variables before developing the trend model. If we estimate a zero coefficient for all secondary damage data, then the trend reduces to a constant mean (the intercept). Note that the estimated coefficients shown in blue in Figure 5a are dependent on the set of field surveyed grids and therefore may differ from the true coefficient estimates as shown in black. These coefficient estimates are also specific to the Nepal earthquake, which was a largely rural disaster; it is not a comment on the general utility of each dataset among all earthquakes. Because the parameters of the trend model are based on its data inputs at the field surveyed locations, G-DIF is calibrated to the data available after each specific earthquake.
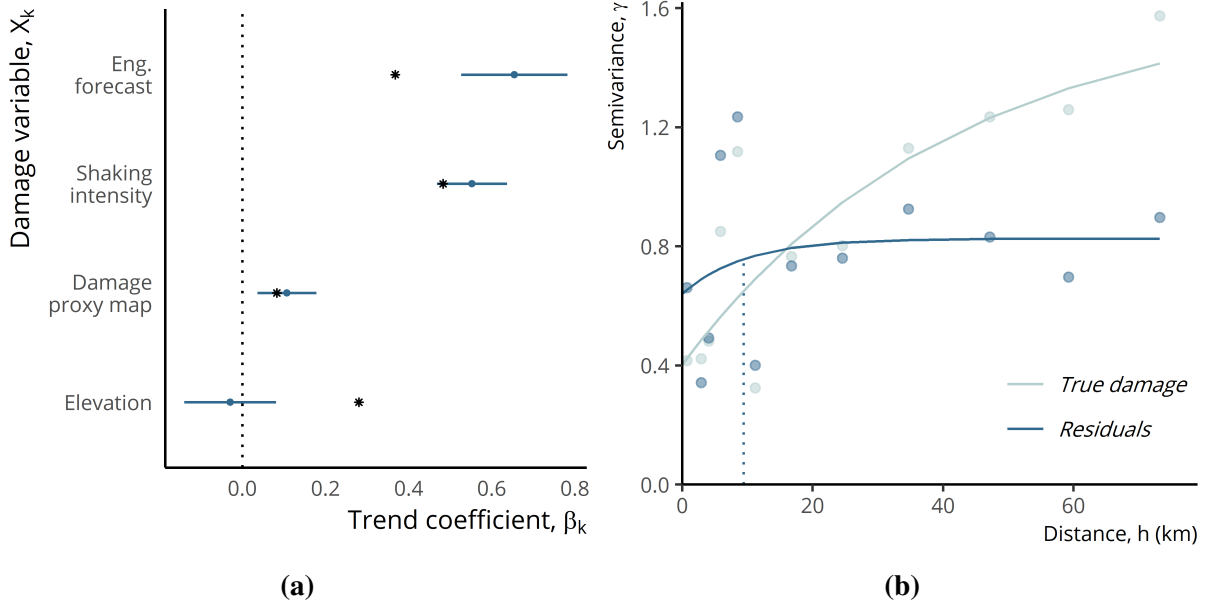
Figure 5. (a) The coefficient estimates (blue dots) from the trend model using ordinary least squares regression in the area with Damage Proxy Map values. Horizontal lines show the standard error and black stars are coefficients using 10000 grids. (b) The spatial correlation model using a Matern variogram showing the difference in the variogram of the true damage at the field surveyed grids and of the variogram of the residuals before and after removing the trend, respectively. The vertical dotted line at 9.4 km highlights the range of spatial autocorrelation.

4. SPATIAL CORRELATION MODEL

Similar to the trend model, the parameters of the spatial correlation model are calibrated to the data rather than predetermined. In this case study, we estimate the parameters of a Matern theoretical variogram model. The fitted parameters when minimizing the residual sum of squares results in an exponential covariance:

$$C(h) = b \exp\left(-\frac{|h|}{r}\right), \tag{11}$$

where b is equal to the variance of the residuals and r is the range of spatial autocorrelation. In this example, we fit these parameters to equal $b = 0.83$ and $r = 9.4$km.

The variogram is related to the covariance through

$$\gamma(h) = b - C(h). \tag{12}$$

We verified the use of this model by comparing the variogram fitted with 100 field surveyed grids shown in Figure 5b to the same model fit with 10,000 grids.

The shape of the variogram highlights spatial characteristics of the data. The vertical dotted line in Figure 5b is the range of spatial autocorrelation, r, of the true damage at the field

16

surveyed locations after removing the trend. The range is the maximum distance at which two locations are spatially autocorrelated with one another. The estimated range of 9.4km is specific to this earthquake and depends on the choice of variogram and fitting procedure, which we evaluate further in the sensitivity analysis in the following section. We evaluate the statistical robustness of the estimated range in the following section. The variogram also shows that we have successfully removed the preexisting trend from the data, since the variogram of the true damage increases with distance, while the variogram of the residuals plateaus. If the trend model were able to fully capture the spatial correlation in the true damage, the variogram would reduce to a horizontal line with $\gamma(0) = \sigma^2(0)$ (i.e. the nugget-effect model), and performing ordinary kriging would provide no additional effect on the final mean damage estimate. Therefore, G-DIF adapts to allow varying levels of contribution from the spatial correlation model, depending on how well the trend model estimates the true damage.

5. FRAMEWORK OUTPUTS

The implementation of G-DIF generates two main outputs: 1) a map of the mean damage estimate for each of the 80,200 grids and 2) a map of uncertainty, or estimation variance, of those estimates.

Damage estimate

The mean damage estimate map (6a) is the sum of the estimated trend and the estimated residuals. The mean damage estimate reflects the trend model such that areas to the north exhibit greater damage than areas to the south. This gradient in damage comes from the two most important secondary damage data in the trend model, the shaking intensity and the engineering forecast, which have higher values towards the north.

The mean damage estimate reflects the spatial correlation model through the similarity in mean damage estimates surrounding the field surveyed locations shown in black in Figure 6a. These spatial similarities are particularly visible to the northeast of Kathmandu, where there is clustering of high damage around the field surveyed points. These similarities are due to the variogram, which estimates small-scale fluctuations based on damage at nearby field surveyed locations.

This map can then be used to estimate total costs of damage. Here, we assume the estimated mean damage grade is the same for all buildings within a grid and that the number of

buildings per grid is known. We use the same replacement costs as Nepal's Post-Disaster Needs Assessment for low-strength masonry, cement-based masonry, and reinforced concrete frame structures of 420000, 1080000, and 6000000 NPR, respectively (Government of Nepal, 2015). We also assume damage grades of 4 or above require full replacement and damage grades 2 and 3 require repair, equaling 10% of the replacement cost. By multiplying the estimated mean damage grade by the number of buildings, an assumed ratio of each type of construction material, and the repair or reconstruction cost for each construction material, we obtain an estimate of 315 billion NPR (2.8 billion USD) for the cost of repair and reconstruction. This estimate is almost the same as the total damages to the housing sector of 303 billion NPR (2.7 billion USD) reported in the PDNA. While this economic loss estimate is not a primary focus of this study, it is provided here to illustrate that these damage predictions can be converted to regional economic loss estimates.

Estimation variance

The map of the estimation variance is the sum of the variance from estimating both the trend and residuals (Equation 9). In the case of least squares regression and ordinary kriging, we solve for the trend coefficients ($\boldsymbol{\beta}$) and kriging weights ($\boldsymbol{\lambda}$) by minimizing the variance of the error at the field surveyed locations. These two procedures result in an estimation variance of the trend and residuals at all locations (specific equations are included in the Electronic Supplement).

We can interpret the estimation variance, $\sigma^2(s)$, as our uncertainty in the mean damage estimate at each grid. The model assumes the uncertainty in the mean damage estimate varies according to a Gaussian probability distribution with $\hat{Z}(s)$ as the mean and $\hat{\sigma}^2(s)$ as the standard deviation—$Z(s) \sim N(\hat{Z}(s), \hat{\sigma}(s))$. The variance quantifies the uncertainty in 1) the trend estimation due to the relationships between the primary and secondary data and 2) spatial estimation of the residuals. The spatial uncertainty is visible in the estimation variance map as shown by the higher variances at grids that are located further from the field survey locations in Figure 6b.

The map of the estimation variance can be used to guide where future field surveys should be carried out and to propagate uncertainty when estimating further losses. Since the variance depends on the location of the field surveyed grids, surveyors could assess damage in areas with higher variance to reduce the overall uncertainty.
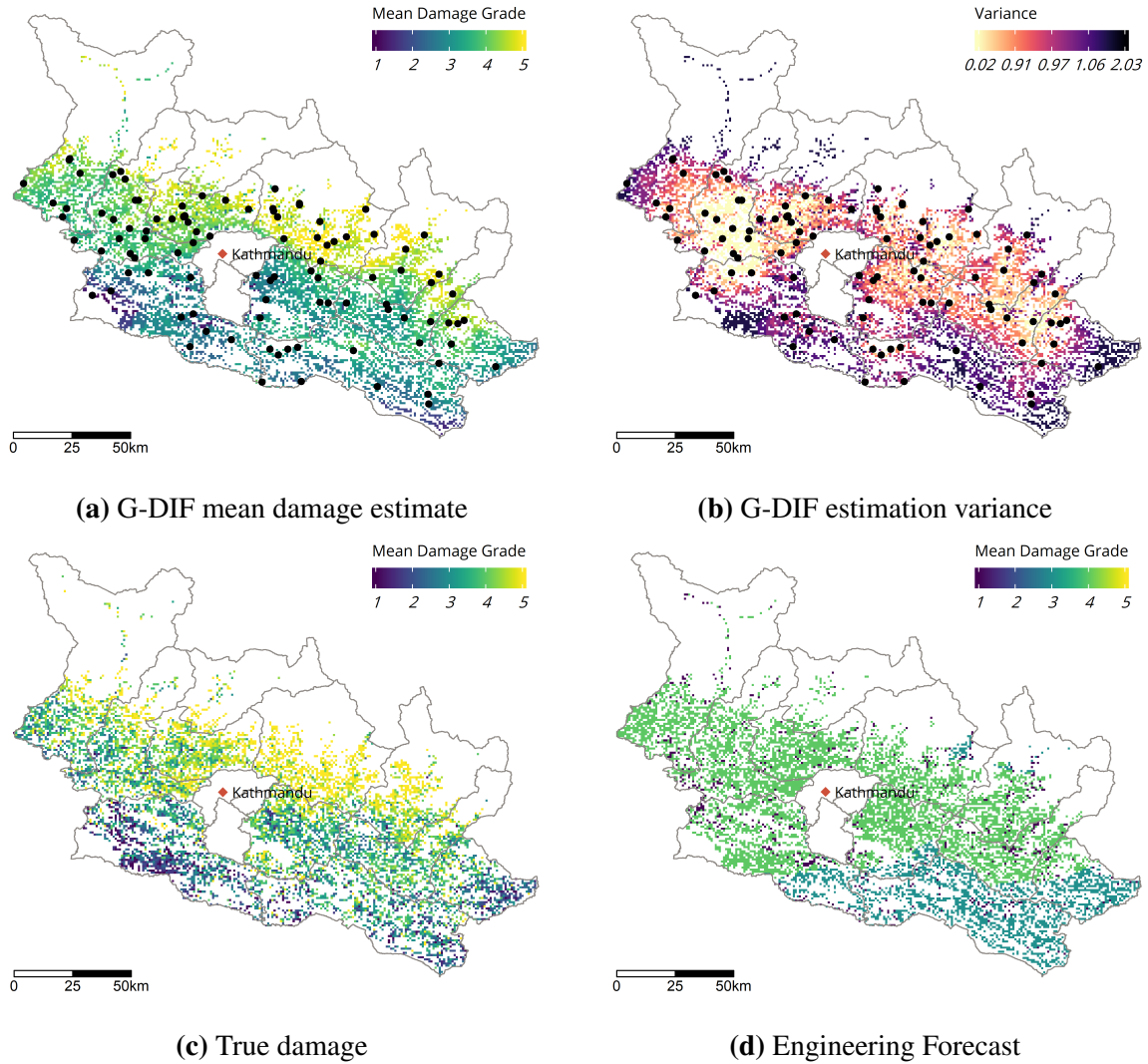
Figure 6. Results of the framework for an example set of 100 field surveyed locations including (a) the mean damage estimate and (b) the estimation variance. The results of (a) can be compared to (c) the true damage from all field surveys and (d) the engineering forecast converted to mean damage grade.

COMPARING G-DIF WITH A RAPID ENGINEERING FORECAST

In this section, we compare G-DIFs spatially varying damage estimate and variance to the engineering forecast, which is the current standard of practice for estimating post-earthquake damage. Visually, we can see that G-DIFs mean damage estimate from the example set of 100 field surveyed grids presented in the previous section (Figure 6a) resembles the true damage (Figure 6c) more than the engineering forecast (Figure 6d). Going further, we quantify the performance of G-DIFs outputs to demonstrate that its mean damage estimate has lower total error and improved uncertainty quantification. Since G-DIF heavily depends on the field survey data, we also perform a sensitivity analysis of G-DIFs outputs to the number and placement of field

surveyed locations used to build the model.

PERFORMANCE OF THE CASE STUDY EXAMPLE

Using the mean damage estimate from the previous case study, we quantify the error between
the predicted and observed damage at all validation grids, as shown in Figure 7a. The distribu-
tion of prediction error highlights 1) the bias, or the mean error—whether the damage estimate
is systematically under or overestimating damage, and 2) the variance, how precise the damage
estimate is for all grids. Note that the engineering forecast only results in mean damage grade
values that are whole integers (1, 3, and 4) after binning the predicted mean damage ratio per
grid, leading to spikes in its errors at whole integers in Figure 7a. The lower bias and variance
of G-DIFs mean damage estimate leads to a mean squared error (MSE), a performance metric
which combines both bias and variance, of MSE = 0.853—47% lower than the engineering
forecast with MSE = 1.62.
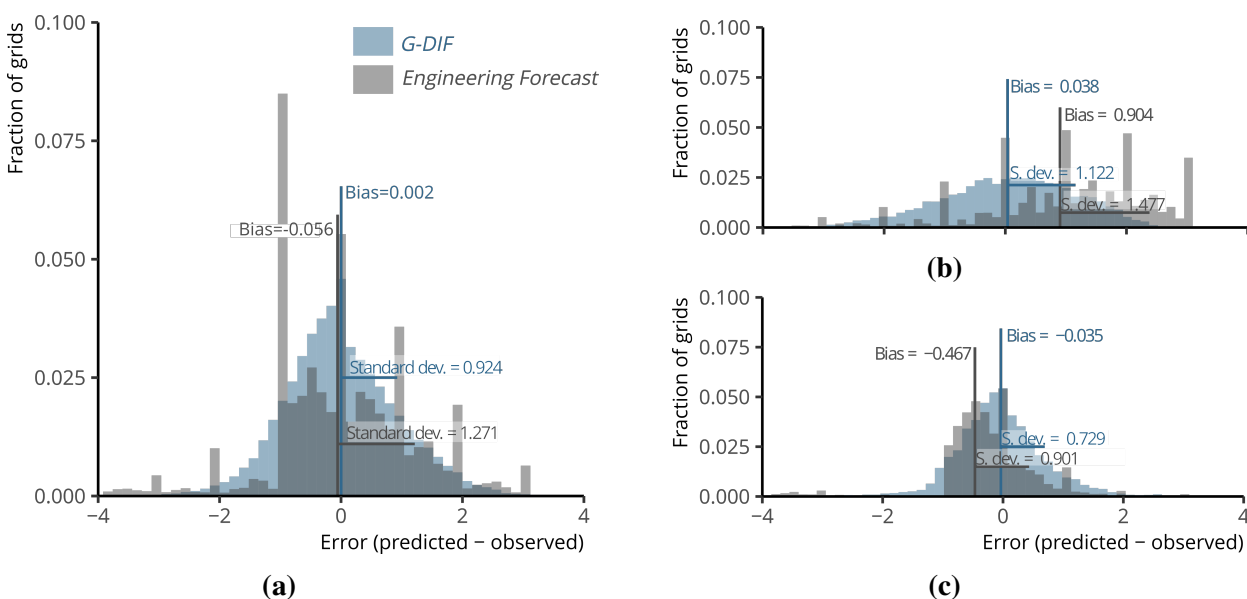
Figure 7. Histogram of errors between the predicted and observed damage for a) all 11 considered
districts, b) Makawanpur district (southwest of Kathmandu Valley), and c) Nuwakot district (northwest
of Kathmandu Valley). Histograms highlight the lower bias, variance, and mean squared error for G-DIF
when using an example set of 100 field surveyed grids.

Even though G-DIFs MSE is nearly half that of the engineering forecast, we see the dif-
ference is even larger when looking at individual districts within the study area (Figure 7b and
c). Over the full study area, the engineering forecast will capture the overall trend in damage
over large regions, but is limited by the resolution of the underlying building inventory data,

20

which is only available at the district-level. G-DIFs advantage over the forecast is that it is locally calibrated to field surveys within a district, so its mean damage estimates for smaller regions have lower bias, variance, and MSE. For example, G-DIFs mean damage estimate has a lower bias (bias = 0.038) and higher precision (standard deviation = 1.122) than that of the engineering forecast (bias = 0.904, standard deviation = 1.477) when considering the errors only for Makawanpur, the district directly southwest of Kathmandu Valley (Figure 7b). G-DIF is consistently more accurate at the local-level for 9 out of the ll districts, as seen in the error histogram for Nuwakot in Figure 7c and the other districts depicted in the electronic supplement.

SENSITIVITY OF THE PERFORMANCE TO THE FIELD SURVEYED GRIDS

G-DIFs final mean damage estimate varies depending upon the sampled primary data, especially with few field survey grids to build the trend and spatial correlation models or with secondary data that are not strongly predictive of damage. The goal of this section is to quantify how G-DIF's performance depends on the number and placement of the field surveyed locations used to build the framework. For a set of field surveyed locations ranging from 25 to 1000, we simulate G-DIFs mean damage estimate using 1000 random samples of different placements and assess its performance. Figure 8 shows the distribution of the MSE and bias for each of these simulations.
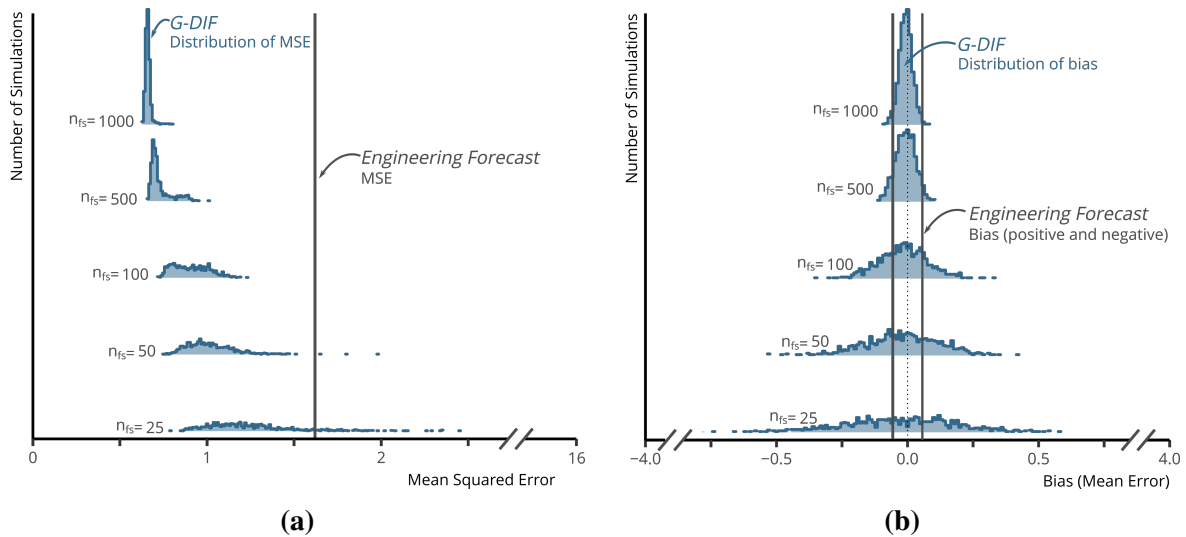
Figure 8. Histograms of (a) the accuracy of the mean damage estimate (MSE) and (b) the performance of the estimation variance from the sensitivity analysis of the number and placement of field surveyed locations used to develop G-DIF. As more field surveys are collected, the accuracy improves and does not depend as much on the placement of field surveyed locations.

21

As expected, as the number of field surveyed locations increases, the G-DIF MSE decreases (accuracy increases) and is consistently lower than that of the engineering forecast, regardless of the placement of the field surveyed locations. Given that the MSE can take values between 0 and 16, the MSE from G-DIF is relatively low. Figure 8a shows histograms of MSE for repeated analyses using varying samples of data, and for five amounts of sampled data. G-DIF MSE is lower than that of the engineering forecast for 99.7 % of the simulations when using 50 field surveyed grids, and the percentage is even higher when more survey locations are used.

When we separate the bias from the MSE, we see that G-DIF distribution of bias is low relative to the full range of possible bias (-4 to 4). The G-DIF damage prediction can result in a more biased result than the engineering forecast, as shown by the areas of the distributions of bias outside of the vertical bounds of the engineering forecasts mean error in Figure 8b. This is partly due to the fact that G-DIFs mean damage estimate depends on how representative the field survey set is of the true distribution of damage. With more biased field survey sets, the final estimate is more biased, but sample bias can be avoided with a sufficiently large field survey if the field survey comes from a random sample. With 500 field survey locations, 86% of the simulations are less biased than the engineering forecast.

G-DIF is more biased than the engineering forecast, also because the forecast has a low mean error of -0.056 for the full study region, as discussed in the previous section. However, the sensitivity analysis confirms G-DIF is more precise when considering sub-regions. Since the MSE is the sum of the variance and squared bias, the reduction in MSE with more field surveyed locations in Figure 8a is due to the reduction in variance of the error. This reduction in variance means that grid-level estimates become more precise. So overall, there is lower variation in the error considering the high resolution of G-DIF's mean damage estimate.

We also evaluated the statistical robustness of the estimate of the range of spatial autocorrelation. After 1000 simulations using 1000 field surveyed locations, the range of the unexplained damage is on average 14 km. This range is consistent with the range of 15-20km reported for damage ratios from the 1994 Northridge earthquake (Shome et al., 2012) and plausible given that the range of spatial correlation for ground motion intensities can vary between 10-60km (Jayaram and Baker, 2009).

WHICH DAMAGE ESTIMATION APPROACH TO USE?

By comparing to the engineering forecast, we show that G-DIF provides a credible damage estimate to support post-earthquake decisions. Whether G-DIF is advantageous over using traditional methods to rapidly estimate damage depends on the amount of primary field data, the quality of the secondary data, and the scale at which decisions are made. In cases where a well-calibrated engineering forecast is available, the study region is large, or there are few field surveyed grids, the engineering forecast will provide reasonable damage estimates.

Often, however, the engineering forecast may be a general model rather than one calibrated for the specific region, or the input inventory data may be of low quality and resolution. In such cases, if there are sufficient field surveys available, G-DIF will likely provide a damage estimate that is comparable or have higher accuracy than that of an engineering forecast. This is because of the approaches' ability to calibrate an event-specific prediction and to also perform spatial interpolation between survey points. In this formulation, we consider measurements from the field to be exact

A main advantage of G-DIF is that it provides locally accurate damage estimates that can be leveraged for loss estimates and higher resolution decisions. This means that within sub-regions, G-DIFs damage estimate will calibrate the engineering forecast, and other secondary damage data, to the field surveys within that region (as seen in the error histogram for Makawanpur district in Figure 7b). To improve the local accuracy of the damage estimate, surveyors can use the uncertainty estimate to guide the collection of additional damage assessments. By surveying in areas with greater uncertainty, the overall uncertainty of the damage estimate will decrease.

CONCLUSION

In this study, we propose a geospatial data integration framework (G-DIF) to produce a spatial damage prediction in the weeks after an earthquake. G-DIF uses a limited sample of local and accurate field surveys to calibrate predictions based on heterogeneous and uncertain damage data from engineering forecasts, remote sensing and other sources. The uncertain data can arrive in varying formats, measurement units, and levels of accuracy.

The geostatistical technique, regression kriging, applied in G-DIF consists of two models. The first is a trend model that estimates the mean damage, a deterministic value that varies in space, using secondary damage data. The second is a spatial correlation model that esti-

mates the stochastic and spatially correlated residuals between the estimated trend and the true damage. The separate modeling of these two components allows the framework to produce a sophisticated trend model when the secondary data is strongly predictive, plus a spatial inter-polation between observations when the secondary damage data has less predictive power. The framework is flexible to implement—the modeler can choose the functional form of the trend prediction (linear or nonlinear) and spatial correlation (variogram) model, depending on the data available for the event of interest.

Data collected after the 2015 Nepal earthquake was used to demonstrate the implementation of G-DIF. Out of 80,200 grids in our area of interest, we used a sample of 100 grids as an example of field surveyed locations and found that the mean damage estimated at the other 80,100 grids had a higher accuracy (lower mean squared error) than a benchmark based on a current engineering forecast. Moreover, G-DIF provides a mean damage estimate that is more accurate for smaller regions than the engineering forecast used in this study, because it locally calibrates all secondary data to field surveys. Modelers can then use this spatially varying mean damage estimate to calculate costs of repair and reconstruction.

In addition to the mean damage estimate map, G-DIF creates a map of the estimation un-certainty, which is important for interpreting results, and a significant addition to the current state of practice for standard damage maps from engineering forecasts or remote sensing dam-age data (e.g. Jaiswal and Wald, 2011; Yun et al., 2015; Copernicus Emergency Management Service, 2019). Post-disaster modelers or decision-makers can use this estimation variance to propagate uncertainty into further impact models or decide where to collect more field surveys to reduce the uncertainty.

With this method we do not explicitly account for uncertainty in the field surveyed assess-ment that results from survey subjectivity and aggregation per grid. The subjectivity in the field surveyed measurement has the potential to be mitigated Booth et al. (2011), so we have made the assumption that its uncertainty is negligible relative to other data sources. This frame-work can be extended to address the uncertainty due to aggregation through Bayesian updating of the damage estimate per grid, similar to that presented in Booth et al. (2011), though this would require estimates of prior and posterior distributions for each dataset and would be more computationally intensive.

With even a small amount of field survey data, G-DIF predictions have improved accuracy relative to standard engineering forecasts. Through Monte Carlo simulations of the number and

locations of field surveys, we found that G-DIF consistently resulted in a damage map with lower mean squared error than an engineering forecast when using more than 50 field surveyed locations. Given that we predict the damage at 80,150 grid locations using 50 field surveyed locations, our framework required 0.06% percent of the grids to be surveyed to improve the estimate of an engineering forecast. In the case of Nepal, 50 field surveyed locations could contain between 250-1150 buildings, which could be feasibly assessed within the first 2-4 weeks in remote, mountainous contexts. While this timeframe may seem long, a few weeks is a sufficient amount of time for this approach to inform important decisions, such as the PDNA which is a major use case.

While our results show an improved mean damage estimate with a small percentage of field surveyed buildings, the placement of field surveys influence these results. Through the sensitivity analysis of the framework to the field surveyed locations, we found G-DIF's mean damage estimate depends on how well the field survey set represents the full damage distribution. A biased set of field surveyed locations can lead to biased results—in the case of the Nepal earthquake, sets of more than 500 grids were less likely to be biased. To develop the spatial correlation model at low separation distances, the field survey set should also consist of locations within the spatial correlation range. To collect field data suited for G-DIF, surveys can be strategically placed to collect damage assessments for all buildings within selected grids so the sample has the full distribution of damage and sufficient spatial coverage, similar to the methods of the REACH survey (e.g. REACH, 2014).

The advantage of G-DIF over standard damage estimates, such as the engineering forecast, is apparent from the Nepal case study. The Nepal earthquake affected a large, mostly rural, region over multiple districts. In this case, secondary data was uncertain because the engineering forecast was developed using low-fidelity data and the damage proxy map was observing changes to both the built environment and vegetation. We expect many future earthquakes to be similar in that there will be a limited sample of accurate field data to calibrate damage predictions from multiple uncertain data. Therefore, the framework presented here could be extended through testing with earthquakes occurring in different built environments or even other types of disasters, as suggested in (Shome et al., 2012).

Overall, the outputs of this framework are useful for stakeholders involved in post-disaster loss assessments (like the PDNA) or recovery aid allocation, such as the affected national government, multilateral or bilateral donor agencies, or civil society organizations. In post-disaster

settings, these stakeholders are often overloaded with making many decisions based on the uncertain data that are available at that time. By combining multiple data, this framework automatically weights those damage datasets according to their ability to predict damage observed in the field surveys, and synthesizes them to develop one map of damage. Therefore, the framework allows stakeholders to address the hurdle of weighing the reliability of input data versus its availability, so they can ultimately make more informed decisions to for a more effective regional recovery.

ELECTRONIC SUPPLEMENT

The data and R code to develop all results for the Nepal case study example presented in this paper are available at https://purl.stanford.edu/gn368cq4893 with an interactive notebook of the code at https://sabineloos.github.io/GDIF-damageprediction/GDIF_nb.html.

ACKNOWLEDGMENTS

REFERENCES

Applied Technology Council, 1989. *Procedures of Postearthquake Safety Evaluation of Buildings. Tech. rep.*, Applied Technology Council, Redwood City, CA.

Bhattacharjee, G., Barns, K., Loos, S., Lallemant, D., Deierlein, G., and Soden, R., 2018. Developing a User-Centric Understanding of Post-Disaster Building Damage Information Needs. In *11th U.S. National Conference on Earthquake Engineering*. Los Angeles, CA.

Boore, D. M., Gibbs, J. F., Joyner, W. B., Tinsley, J. C., and Ponti, D. J., 2003. Estimated Ground Motion From the 1994 Northridge , California , Earthquake at the Site of the Interstate 10 and La Cienega Boulevard, West Los Angeles, California. *Bulletin of the Seismological Society of America* **93**, 2737–2751.

Booth, E., Saito, K., Spence, R., Madabhushi, G., and Eguchi, R. T., 2011. Validating Assessments of Seismic Damage Made from Remote Sensing. *Earthquake Spectra* **27**, S157–S177.

Bright, E. A., Coleman, P. R., Rose, A. N., and Urban, M. L., 2012. LandScan 2011. Oak Ridge National Laboratory.

Chatterjee, A., Michalak, A. M., Kahn, R. a., Paradise, S. R., Braverman, A. J., and Miller, C. E., 2010. A geostatistical data fusion technique for merging remote sensing and ground-based observations of aerosol optical thickness. *Journal of Geophysical Research* **115**, 1–12. doi:10.1029/2009JD013765.

Chiles, J.-P. and Delfiner, P., 2012. *Geostatistics: Modeling Spatial Uncertainty*. 2 edn. Wiley Series in Probability and Statistics, New York, NY. ISBN 978-0471083153, 734 pp.

Copernicus Emergency Management Service, 2019. Rapid Mapping Portfolio.

Corbane, C., Saito, K., DellOro, L., Bjorgo, E., Gill, S., Boby, P., Huyck, C., Kemper, T., Lemoine, G., Spence, R., Shankar, R., Senegas, O., Ghesquiere, F., Lallemant, D., Evans, G., Gartley, R., Toro, J., Ghosh, S., Svekla, W., Adams, B., and Eguchi, R. T., 2011. A Comprehensive Analysis of Building Damage in the 12 January 2010 Mw7 Haiti Earthquake Using High-Resolution Satellite and Aerial Imagery. *Photogrammetric Engineering Remote Sensing* **77**, 997–1009.

Dong, L. and Shan, J., 2013. A comprehensive review of earthquake-induced building damage detection with remote sensing techniques. *ISPRS Journal of Photogrammetry and Remote Sensing* **84**, 85–99.

Earthquake Engineering Research Institute, 2015. *Learning From Earthquake (LFE) Program. Tech. rep.*, Earthquake Engineering Research Institute, Oakland, CA.

Erdik, M., Sesetyan, K., Demircioglu, M., Zulfikar, C., Hancilar, U., Tuzun, C., and Harmandar, E., 2014. Rapid Earthquake Loss Assessment After Damaging Earthquakes. In *Geotechnical, Geological and Earthquake Engineering*, vol. 34, pp. 53–96. ISBN 9783319071176. doi: 10.1007/978-3-319-07118-3.

Farr, T. G., Rosen, P. A., Caro, E., Crippen, R., Duren, R., Hensley, S., Kobrick, M., Paller, M., Rodriguez, E., Roth, L., Seal, D., Shaffer, S., Shimada, J., Umland, J., Werner, M., Oskin, M., Burbank, D., and Alsdorf, D. E., 2007. The shuttle radar topography mission. *Reviews of Geophysics* **45**. doi:10.1029/2005RG000183.

Ghosh, S., Huyck, C. K., Greene, M., Gill, S. P., Bevington, J., Svekla, W., DesRoches, R., and Eguchi, R. T., 2011. Crowdsourcing for Rapid Damage Assessment: The Global Earth Observation Catastrophe Assessment Network (GEO-CAN). *Earthquake Spectra* **27**, S179–S198.

Goda, K. and Hong, H. P., 2008. Spatial correlation of peak ground motions and response spectra. *Bulletin of the Seismological Society of America* **98**, 354–365. doi:10.1785/0120070078.

Government of Nepal, 2015. *Nepal Earthquake 2015 Post Disaster Needs Assessment*.

Grujic, O., 2017. Subsurface Modeling with Functional Data. Ph.D. thesis, Stanford University.

Grünthal, G., 1998. *European Macroseismic Scale 1998*, vol. 15. ISBN 2879770084, 100 pp.

Gunasekera, R., Daniell, J., Pomonis, A., Arias, R. A., Ishizawa, O., and Stone, H., 2018. *Methodology Note on the Global RApid post-disaster Damage Estimation (GRADE) approach. Tech. rep.*, Global Facility for Disaster Reduction and Recovery, Washington, DC.

Hengl, T., Heuvelink, G., and Stein, A., 2003. Comparison of kriging with external drift and regression-kriging. *Technical note, ITC* p. 17. doi:10.1016/S0016-7061(00)00042-2.

Hengl, T., Heuvelink, G. B. M., and Stein, A., 2004. A generic framework for spatial prediction of soil variables based on regression-kriging. *Geoderma* **120**, 75–93. doi:10.1016/j.geoderma.2003.08.018.

Hunt, A. and Specht, D., 2019. Crowdsourced mapping in crisis zones: collaboration, organisation and impact. *Journal of International Humanitarian Action* **4**, 1–11. doi:10.1186/s41018-018-0048-1.

Huyck, C. K., 2015. Gorkha (Nepal) Earthquake Response.

Jaiswal, K., Wald, D., and Hearne, M., 2009. *Estimating casualties for large earthquakes worldwide using an empirical approach: US geological survey open-file report, OF 2009-1136, 78 p. Tech. rep.*

Jaiswal, K. and Wald, D. J., 2011. *Rapid Estimation of the Economic Consequences of Global Earthquakes. Tech. rep.*, USGS, Reston, VA.

James, G., Witten, D., Hastie, T., and Tibshirani, R. J., 2013. *An Introduction to Statistical Learning*. Springer, New York, NY. ISBN 9781461471370, 1–440 pp.

Jarvis, A., Reuter, H. I., Nelson, A., and Guevara, E., 2008. Hole-filled seamless SRTM data V4.

Jayaram, N. and Baker, J., 2009. Correlation model for spatially distributed ground-motion intensities. *Earthquake Engineering {&} Structural Dynamics {...}* .

JICA, 2002. *The study on earthquake disaster mitigation in the Kathmandu Valley, Kingdom of Nepal. Tech. rep.*, Japan International Cooperation Agency : Nippon Koei Co., Ltd. : Oyo Corp.

Kerle, N., 2013. Remote Sensing Based Post-Disaster Damage Mapping with Collaborative Methods. *Intelligent Systems for Crisis Management* pp. 121–133. doi:10.1007/978-3-642-33218-0.

Kerle, N. and Hoffman, R. R., 2013. Collaborative damage mapping for emergency response : the role of Cognitive Systems Engineering. *Natural hazards and earth system sciences* **13**, 97–113.

Lallemant, D. and Kiremidjian, A., 2013. Rapid post-earthquake damage estimation using remote-sensing and field-based damage data integration. In *Safety, Reliability, Risk and Life-Cycle Performance of Structures and Infrastructures*, pp. 3399–3406. CRC Press.

Lallemant, D., Soden, R., Rubinyi, S., Loos, S., Barns, K., and Bhattacharjee, G., 2017. Post-Disaster Damage Assessments as Catalysts for Recovery: A Look at Assessments Conducted in the Wake of the 2015 Gorkha, Nepal, Earthquake. *Earthquake Spectra* **33**, S435–S451. doi:10.1193/120316EQS222M.

Loos, S., Barns, K., Bhattacharjee, G., Soden, R., Herfort, B., Eckle, M., Giovando, C., Girardot, B., Saito, K., Deierlein, G., Kiremidjian, A., Baker, J. W., and Lallemant, D., 2018. *The Development and Uses of Crowdsourced Building Damage Information based on Remote-Sensing. Tech. rep.*, Stanford, CA.

McBratney, A. B., Odeh, I. O., Bishop, T. F., Dunbar, M. S., and Shatar, T. M., 2000. *An overview of pedometric techniques for use in soil survey*, vol. 97. ISBN 0016-7061, 293–327 pp. doi:10.1016/S0016-7061(00)00043-4.

Monfort, D., Negulescu, C., and Belvaux, M., 2019. Remote sensing vs. field survey data in a post-earthquake context: Potentialities and limits of damaged building assessment datasets. *Remote Sensing Applications: Society and Environment* **14**, 46–59. doi:10.1016/j.rsase.2019.02.003.

Motaghian, H. R. and Mohammadi, J., 2011. Spatial estimation of saturated hydraulic conductivity from terrain attributes using regression, kriging, and artificial neural networks. *Pedosphere* **21**, 170–177. doi:10.1016/S1002-0160(11)60115-X.

Nepal Earthquake Housing Reconstruction Multi-Donor Trust Fund, 2016. *Nepal Earthquake Housing Reconstruction Annual Report. Tech. rep.*, Nepal Earthquake Housing Reconstruction Multi-Donor Trust Fund, Kathmandu, Nepal.

Odeh, I. O. A., McBratney, A. B., and Chittleborough, D. J., 1994. Spatial prediction of soil properties

from landform attributes derived from a digital elevation model. *Geoderma* **63**, 197–214. doi:10.1016/0016-7061(94)90063-9.

Oliver, M. A. and Webster, R., 2014. A tutorial guide to geostatistics: Computing and modelling variograms and kriging. *Catena* **113**, 56–69. doi:10.1016/j.catena.2013.09.006.

REACH, 2014. *Groundtruthing Open Street Map Building Damage Assessment: Haiyan Typhoon - The Philippines*. Tech. Rep. April, REACH; American Red Cross; USAID.

Shelter Cluster Nepal, 2015. *Shelter and Settlements Vulnerability Assessment: Nepal 25 April / 12 May Earthquakes Response Nepal*. Tech. Rep. June, Shelter Cluster Nepal, Nepal.

Shome, N., Jayaram, N., and Rahnama, 2012. Uncertainty and Spatial Correlation Models for Earthquake Losses. In *15th World Conference on Earthquake Engineering (15WCEE)*, p. 10. Lisbon, Portugal.

Thompson, E. M., Baise, L. G., Kayen, R. E., Tanaka, Y., and Tanaka, H., 2010. A geostatistical approach to mapping site response spectral amplifications. *Engineering Geology* **114**, 330–342.

Trendafiloski, G., Wyss, M., and Rosset, P., 2009. Loss Estimation Module in the Second Generation Software QLARM. In *Second International Workshop on Disaster Casualties*, June, pp. 1–10. Cambridge, UK. ISBN 9789048194551. doi:10.1007/978-90-481-9455-1.

United Nations Office for the Coordination of Humanitarian Affairs, 2019. ReliefWeb - Informing humanitarians worldwide.

Université catholique de Louvain (UCL) - CRED and Guha-Sapir, D., . EM-DAT: The Emergency Events Database.

Wald, D. J., Jaiswal, K. S., Marano, K. D., Garcia, D., So, E., and Hearne, M., 2012. Impact-Based Earthquake Alerts with the U. S. Geological Surveys PAGER System: What's Next? In *15th World Conference on Earthquake Engineering, Lisbon Portugal*.

Westrope, C., Banick, R., and Levine, M., 2014. Groundtruthing OpenStreetMap Building Damage Assessment. *Procedia Engineering* **78**, 29–39.

Worden, C. B., Thompson, E. M., Baker, J. W., Bradley, B. A., Luco, N., and Wald, D. J., 2018. Spatial and Spectral Interpolation of GroundMotion Intensity Measure Observations. *Bulletin of the Seismological Society of America* doi:10.1785/0120170201.

Worden, C. B. and Wald, D., 2016. *ShakeMap Manual. Tech. rep.*

Yun, S.-h., Hudnut, K., Owen, S., Webb, F., Sacco, P., Gurrola, E., Manipon, G., Liang, C., Fielding, E., Milillo, P., Hua, H., and Coletta, A., 2015. Rapid Damage Mapping for the 2015 M w 7 . 8 Gorkha Earthquake Using Synthetic Aperture Radar Data from COSMO SkyMed and ALOS-2 Satellites. *Seismological Research Letters* **86**, 1549–1556. doi:10.1785/0220150152.